

Transient Absorption of Warm Dense Matter Created by an X-Ray Free-Electron Laser

Laurent Mercadier (✉ laurent.mercadier@xfel.eu)

European XFEL <https://orcid.org/0000-0003-0606-0461>

Andrei Benediktovitch (✉ andrei.benediktovitch@cfel.de)

Center for Free-Electron Laser Science CFEL, Deutsches Elektronen-Synchrotron DESY

Spela Krusic (✉ spela.krusic@ijs.si)

J. Stefan Institute

J. Schlappa (✉ justine.schlappa@xfel.eu)

European X-Ray Free Electron Laser Facility GmbH

Marcus Agåker (✉ marcus.agaker@physics.uu.se)

Uppsala University

Robert Carley (✉ robert.carley@xfel.eu)

European XFEL

Giuseppe Fazio (✉ giuseppe.fazio@phys.chem.ethz.ch)

ETH Zürich

Natalia Gerasimova (✉ natalia.gerasimova@xfel.eu)

European X-Ray Free Electron Laser

Young Yong Kim (✉ kimyy@postech.ac.kr)

Pohang Accelerator Laboratory

Loïc Le Guyader (✉ loic.le.guyader@xfel.eu)

Helmholtz-Zentrum Berlin für Materialien und Energie GmbH <https://orcid.org/0000-0002-5731-3724>

Giuseppe Mercurio (✉ giuseppe.mercurio@xfel.eu)

European XFEL GmbH, Schenefeld <https://orcid.org/0000-0003-4221-6670>

Sergii Parchenko (✉ sergii.parchenko@xfel.eu)

European XFEL

Jan-Erik Rubensson (✉ jan-erik.rubensson@physics.uu.se)

Uppsala University <https://orcid.org/0000-0003-1467-8114>

Svitozar Serkez (✉ svitozar.serkez@xfel.eu)

European XFEL

Michal Stransky (✉ michal.stransky@xfel.eu)

European XFEL

Martin Teichmann (✉ martin.teichmann@xfel.eu)

European XFEL <https://orcid.org/0000-0003-4215-9792>

Zhong Yin (✉ zhong.yin.e2@tohoku.ac.jp)

European XFEL

Matjaz Žitnik (✉ matjaz.zitnik@ijs.si)

Jožef Stefan Institute

Andreas Scherz (✉ andreas.scherz@xfel.eu)

European X-Ray Free Electron Laser

Beata Ziaja-Motyka (✉ ziaja@mail.desy.de)

Center for Free-Electron Laser Science <https://orcid.org/0000-0003-0172-0731>

Nina Rohringer (✉ nina.rohringer@desy.de)

Max Planck Advanced Study Group <https://orcid.org/0000-0001-7905-3567>

Article

Keywords:

DOI: <https://doi.org/>

License:   This work is licensed under a Creative Commons Attribution 4.0 International License.

[Read Full License](#)

Additional Declarations: There is **NO** Competing Interest.

Transient Absorption of Warm Dense Matter Created by an X-Ray Free-Electron Laser

Laurent Mercadier,^{1,*} Andrei Benediktovitch,² Špela Krušič,³ Justine Schlappa,¹
Marcus Agåker,^{4,5} Robert Carley,¹ Giuseppe Fazio,⁶ Natalia Gerasimova,¹ Young
Yong Kim,¹ Loïc Le Guyader,¹ Giuseppe Mercurio,¹ Sergii Parchenko,¹ Jan-Erik
Rubensson,⁴ Svitozar Serkez,¹ Michal Stransky,^{1,7} Martin Teichmann,¹ Zhong
Yin,^{1,†} Matjaž Žitnik,³ Andreas Scherz,¹ Beata Ziaja,^{2,7,‡} and Nina Rohringer^{2,8}

¹*European XFEL, 22869 Schenefeld, Germany*

²*Center for Free-Electron Laser Science CFEL,
Deutsches Elektronen-Synchrotron DESY,
Notkestr. 85, 22607 Hamburg, Germany*

³*Jožef Stefan Institute, 1000 Ljubljana, Slovenia*

⁴*Department of Physics and Astronomy, Uppsala University,
P.O. Box 516, SE-751 20 Uppsala, Sweden*

⁵*MAX IV Laboratory, Lund University,
PO Box 118, SE-22100 Lund, Sweden*

⁶*Laboratorium für Physikalische Chemie,
ETH Zürich, 8093 Zürich, Switzerland*

⁷*Institute of Nuclear Physics, Polish Academy of Sciences,
Radzikowskiego 152, 31-342 Krakow, Poland*

⁸*Universität Hamburg, 22607 Hamburg, Germany*

Abstract

Warm dense matter (WDM) is a ubiquitous state of matter encountered in various high energy density environments, at the frontier between a plasma and a condensed phase. It is key to astrophysics, planetary science and inertial confinement fusion research, but its electronic and ionic structure and dynamics remain poorly understood. Here, an intense and ultrafast X-ray free electron laser (XFEL) pulse is used to simultaneously create and characterize warm dense copper via L -edge X-ray absorption spectroscopy. The rich electron dynamics occurring within the 15-femtosecond pulse duration are revealed over a large irradiation intensity range. Below $10^{15} \text{ W cm}^{-2}$, an absorption peak below the L -edge appears, originating from the depletion of the $3d$ band, and shows a distinct energy redshift with increasing intensity. This shift is a possible signature of ionization potential depression and electronic bond hardening. At higher intensities, massive ionization and collisions lead to the transition from reverse saturable absorption (opening absorption channels) to saturable absorption (material bleaching) of the XFEL pulse, an effect that holds promise for X-ray pulse shaping. The presented method is applicable to a wide range of materials and constitutes a robust benchmark for non-equilibrium models of electron dynamics in WDM.

MAIN

Introduction

The interaction between intense X-rays and matter is a new area of science accessible through the development of X-ray free-electron lasers (XFEL). These brilliant and ultrafast sources, in conjunction with strongly focusing optics, are capable of driving solids out of equilibrium, inducing nonlinear effects such as saturable absorption (SA), through which, e.g., a metal transiently becomes transparent [1–4] in specific spectral regions, or its counterpart, reverse saturable absorption (RSA), where its absorption increases with increasing excitation level [5]. SA and RSA are routinely used in the optical regime for applications such as mode-locking, pulse-shaping or two-photon microscopy [6–8], with possible transi-

* laurent.mercadier@xfel.eu

† current address: International Center for Synchrotron Radiation Innovation Smart, Tohoku University, 2-1-1 Katahira, Aoba-ku, Sendai, Miyagi 980-8577, Japan

‡ ziaja@mail.desy.de

tions between these regimes [9, 10]. Thus, SA and RSA open the door to controlled X-ray pulse shaping [2, 11]. In the X-ray spectral region, the intense irradiation can transiently transform the system into warm dense matter (WDM) [12, 13]. In this state, the potential energy of the interaction between electrons and nuclei and the kinetic energy of the electrons become comparable. The temperature of electrons is close to the Fermi temperature. Understanding the physics governing the transition from cold solid to WDM is key to many fields of research including astrophysics, planetary interiors and laboratory-based experiments such as inertial confinement fusion. The characterization of transiently evolving WDM is, however, challenging. So far, X-ray emission spectroscopy (XES) has been a method of choice to reveal its non-equilibrium dynamics [14–17], enabling the estimation of collisional ionization rates [18, 19] and of the ionization potential depression (IPD) [20, 21]. A complementary technique, time-resolved X-ray absorption spectroscopy (XAS), appears as a powerful tool to probe simultaneously the valence electron state and the atomic structure [22]. Until now, XAS was mostly applied to infrared- and optically-heated WDM with picosecond to subpicosecond time resolution [23–28]. This excitation regime, heating valence electrons only, is drastically different from the X-ray regime, in which heating is initiated by ionization of core-shell electrons. So far, most of the few XAS measurements of X-ray irradiated solids [1, 3, 5] were spectrally integrated, thus providing limited information on the underlying structure of WDM.

Here, we take advantage of the large spectral bandwidth of XFEL pulses created by the process of self-amplified spontaneous emission (SASE) to study the formation of warm dense copper via XAS. SASE bandwidths are typically large enough to perform XAS at the absorption edges of most elements [2, 29], giving a unique insight into the transient, non-equilibrium electronic dynamics of the irradiated solids during their evolution towards WDM state. We demonstrate in the X-ray regime the transition from RSA to SA, here at the Cu L_2 (952 eV) and L_3 (932 eV) edges. Such a transition was predicted in aluminum by Cho et al. [5, 30], but it has so far never been observed due to the lack of sufficient XFEL intensity. XAS also reveals the evolution of the electronic system: we observe a negative energy shift of the X-ray-induced pre-edge absorption originating from the $3d$ vacancies that are formed with increasing pulse intensity. This shift is interpreted as a signature of ionization potential depression and electronic bond hardening, as predicted in Refs. [22, 31].

Spectral observations of XFEL-generated WDM

Absorption spectra (see Methods for details) from a 100-nm thick Cu film with XFEL pulses tuned to the L_3 absorption edge are shown in Fig. 1 for various pulse intensities I . For intensities $I \geq 1 \times 10^{13} \text{ W cm}^{-2}$, the absorption increases in the spectral region below the edge. This pre-edge feature is well known [22, 25–28]. It is due to the presence of $3d$ vacancies which trigger photoabsorption through $2p_{3/2} \rightarrow 3d$ transitions. The pre-edge absorption drastically increases with pulse intensity to become 2.5 times larger than the cold L_3 edge amplitude at $I_{tr} = 1 \times 10^{15} \text{ W cm}^{-2}$. This increase is accompanied by a shift towards lower energies, which is discussed in details later. For intensities $I > I_{tr}$ the pre-edge peak broadens, it shifts towards higher photon energies and the overall absorption decreases. At the highest pulse intensity, the L_3 edge can not be clearly resolved. A moderate, monotonic increase of absorption with photon energy is observed across the whole probed energy range.

Another distinct feature of the spectrum is a ~ 1 -eV wide peak centered at 936.7 eV, indicated by the black arrow in Fig. 1. This peak is a signature of a van Hove singularity [32, 33], a singularity in the density of states characteristic for the face centered cubic crystalline phase of solid copper. It was shown to disappear upon melting in an optically excited pump-probe experiment [27], indicating the loss of crystal order [22, 33]. In our case, the pulse duration is so short that no structural change involving ion motion takes place, an assumption corroborated by our observation of the van Hove peak up to intensities of $1 \times 10^{14} \text{ W cm}^{-2}$. Since the spectra are averaged over the entire spatial, nearly Gaussian, intensity profile of the pulse, the presence of the peak may be enhanced by contributions from colder outer regions of the probed sample. At higher intensities, the peak becomes buried in the spectral region of the shifting pre-edge feature. The redistribution of the electronic states is then so strong (see discussions below) that the van Hove singularity of cold copper is no longer a reliable feature to analyze the crystalline structure.

We measured similar series of spectra for 500 nm thickness (Supplementary Information Fig. S2), and at the L_2 edge for 100 nm (Supplementary Information Fig. S3) and 500 nm thicknesses (Supplementary Information Fig. S4). The L_2 and L_3 edges have similar structures [33] with an energy shift of 20 eV, but their intensities differ by a factor of 2 (the statistical branching ratio). In all conditions, we observed similar trends, in particular the transition from RSA to SA, which is described in details below.

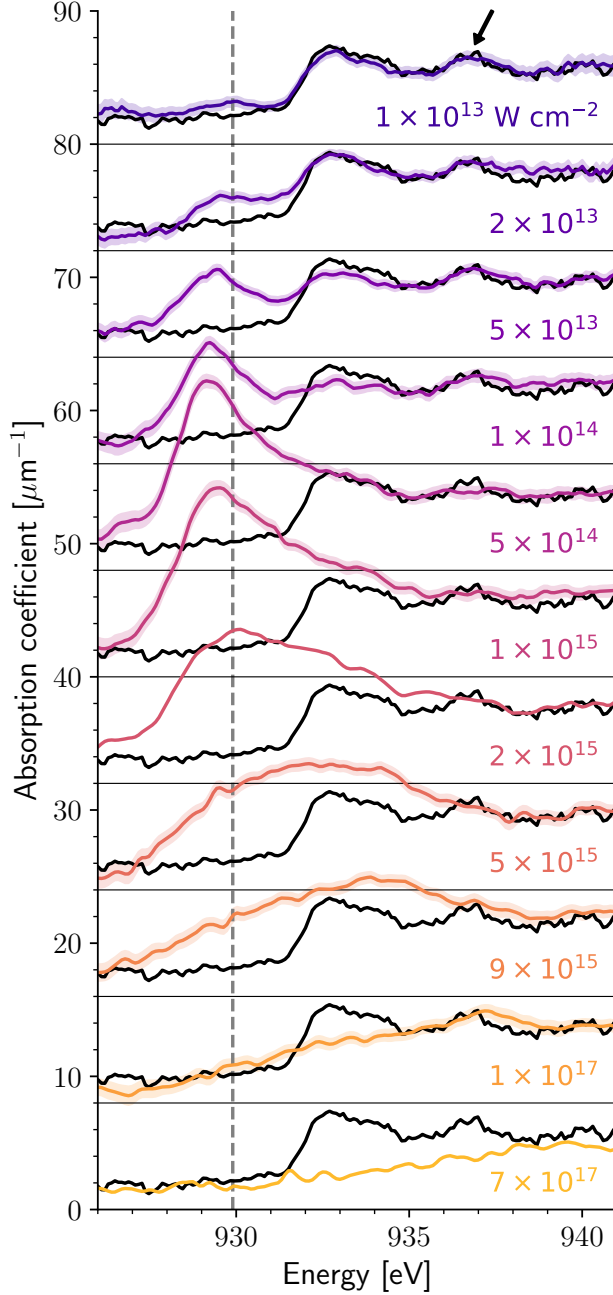


FIG. 1. Transient XAS of XFEL-generated warm dense copper. Absorption spectra of 100 nm thick film at the L_3 edge are shown for various XFEL intensities indicated in the figure. The spectra are offset from each other by $8 \mu\text{m}^{-1}$ for clarity purposes and overlaid with a reference spectrum obtained at $I = 5 \times 10^{12} \text{ W cm}^{-2}$ (black line). The shaded areas around each spectrum indicate the 95% confidence interval. The grey dashed line indicates the peak position of the pre-edge feature at low intensity. The arrow shows the characteristic fcc peak resulting from a van Hove singularity.

111

112 Transition from RSA to SA

113 Fig. 2 (a) shows the XFEL pulse transmission as a function of intensity, exploring a
 114 transition from RSA to SA both at the L_2 and L_3 edges, for Cu films of 100 nm and 500
 115 nm thickness. For the 100 nm sample, the transmission is constant up to an intensity of
 116 $1.6 \times 10^{13} \text{ W cm}^{-2}$ at the L_3 edge and above that it decreases to a minimum at $I_{tr} = 1 \times 10^{15}$
 117 W cm^{-2} (RSA), and then increases again for higher intensities (SA). We observe a similar
 118 behaviour at the L_2 edge, but the characteristic features are shifted to higher intensities,
 119 with the transition from RSA to SA occurring at $I_{tr} = 1 \times 10^{16} \text{ W cm}^{-2}$ (see our theoretical
 120 modelling for an explanation of this effect). For the 500 nm sample, the same RSA to SA
 121 transition is observed, albeit shifted towards higher intensities because of the overall larger
 122 absorption. The transition intensities are $1 \times 10^{16} \text{ W cm}^{-2}$ at the L_3 and $2 \times 10^{16} \text{ W cm}^{-2}$
 123 at the L_2 edge, respectively. Strikingly, the transmission at the L_2 edge is reduced by a
 124 factor of 3 by RSA, and becomes larger by a factor of 6 with respect to that of the cold
 125 sample by SA at $I = 7 \times 10^{17} \text{ W cm}^{-2}$.

126

127 We also follow the spectrally-resolved transition from RSA to SA in Fig. 2 (b)-(e), by
 128 looking at regions centered below, on and above the L_2 and L_3 edges. The transmission
 129 level below the L_3 edge at low intensity is, as expected, close to that of a cold target (87%
 130 for 100 nm [34]). The transition is observed in all considered regions except for region 1
 131 (below the L_3 pre-edge), but the intensity at which it occurs is higher for regions of higher
 132 photon energies. This effect is discussed in detail below.

133

134 Modelling with kinetic Boltzmann approach

135 To get a better understanding of the dynamics within the irradiated copper at the L_3 edge,
 136 we use a kinetic Boltzmann equations solver developed in [35] and adapted in [36, 37]. The
 137 atomistic model follows the non-equilibrium evolution of emerging free-electron densities and
 138 atomic configuration densities resulting from photoexcitations, Auger decays of core holes

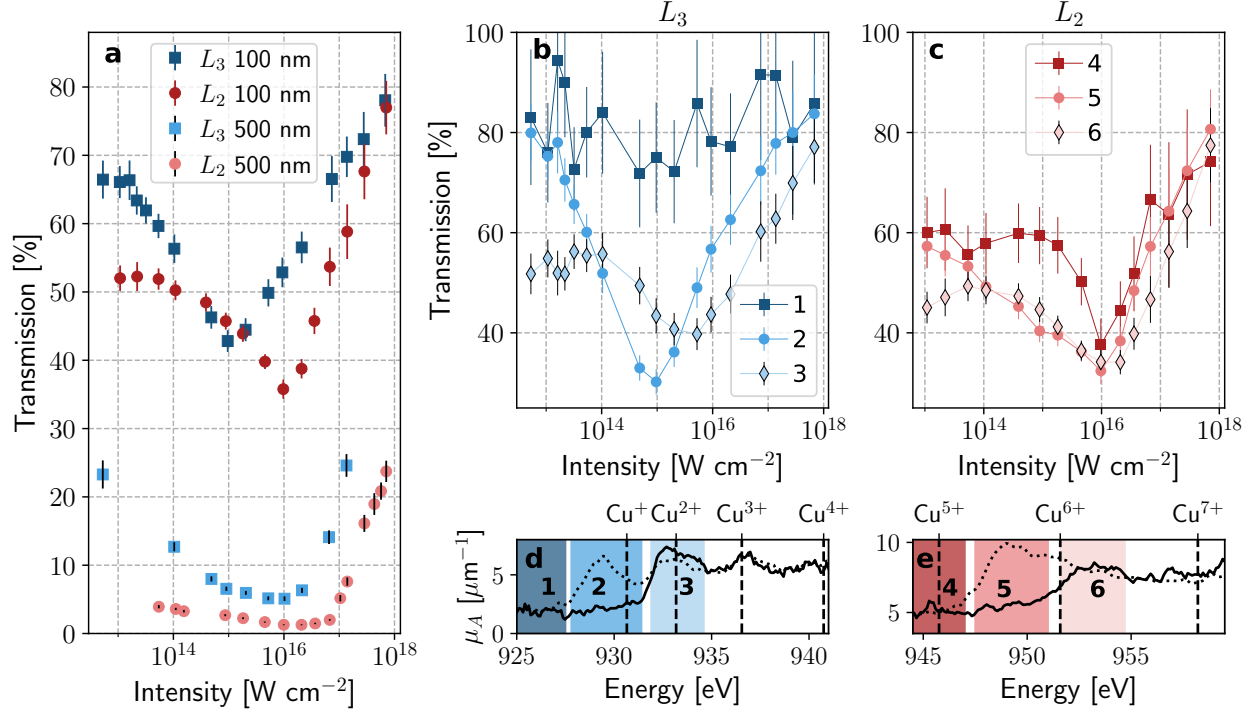


FIG. 2. Transition from RSA to SA. (a): Transmission of a SASE XFEL pulse centered at the Cu L_2 and L_3 edges as a function of pulse intensity and film thickness. In all cases, the transmission first decreases (RSA), reaching a minimum, and then increases (SA) as a function of intensity. (b) and (c): Transmission in selected spectral regions below the L_3 or L_2 pre-edges (1,4), on the L_3 or L_2 pre-edge (2, 5) and on the L_3 or L_2 edge (3, 6), respectively, as shown in corresponding panels (d) and (e), for 100 nm film thickness. The vertical dashed lines in (d) and (e) show, for a given ionic species, the calculated $2p_{3/2} \rightarrow 3d$ transition energy. The solid lines show the cold reference spectra while the dotted lines show spectra where the pre-edge features are prominent, obtained at $I = 5 \times 10^{13} \text{ W cm}^{-2}$ (d) and $I = 9 \times 10^{14} \text{ W cm}^{-2}$ (e), respectively. The error bars in (a), (b) and (c) indicate the 95% confidence interval.

and subsequent electronic collisional processes (see Methods for details). This approach is suited for modeling early-time evolution following X-ray excitation. Since the $3d$ orbitals (the focus of our study) in copper are strongly localized [38], the atomistic picture is justified. For simplicity, we limit the calculations to the case of the 100 nm Cu film irradiated at the L_3 edge. The sample is thin enough to assume uniform heating. Detailed outputs of the model can be found in the Supplementary Information (Figs. S7 - S10). Fig. 3 (a) and (b) show the evolution of the transient electron energy distribution, n_e , for $I = 5 \times 10^{12} \text{ W cm}^{-2}$

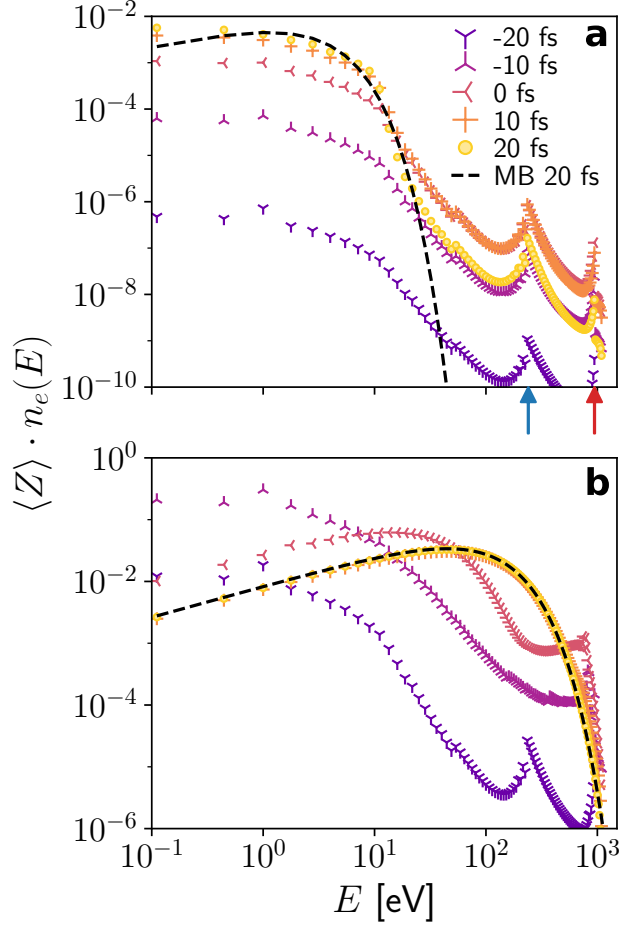


FIG. 3. Evolution of the transient electron energy distribution in XFEL-irradiated Cu with (a): pulse intensity $I = 5 \times 10^{12} \text{ W cm}^{-2}$ and (b): pulse intensity $I = 1 \times 10^{17} \text{ W cm}^{-2}$. The curves represent the normalized electron distributions at various time instants (0 fs corresponding to the maximum of the pulse). They are multiplied by the actual value of the transient ionization degree per atom, $\langle Z \rangle$, i.e., the number of free electrons above the vacuum level divided by the total number of atoms, in order to show the increase of the free electron density per atom in the sample. The dashed curves show the Maxwell-Boltzmann distributions with a kinetic temperature equal to the average electron kinetic energy at 20 fs. The broad peak with substructure at around 250 eV indicated by a blue arrow corresponds to the secondary electron emission during the collisional ionization of neutral Cu and Cu^+ ground states. The sharp peak at 943 eV indicated by a red arrow is due to the Auger decay of the $2p_{3/2}$ core hole.

146 and $I = 1 \times 10^{17} \text{ W cm}^{-2}$. Initially, photo- and Auger electron peaks are visible in the high
 147 energy range of the spectra for both low and high X-ray intensities. At low X-ray intensity,

the electronic distribution below ~ 30 eV increases with time and almost stabilizes after 10 fs, approaching a Maxwell-Boltzmann (M-B) distribution. On the contrary, the high energy contribution to the energy spectra continuously decreases after 0 fs but keeps its peaked structure. This shows that the electronic system is still not equilibrated after the pulse has passed. At high X-ray intensity, the situation is different: the peaks in the high energy range are quickly redistributed between -20 and -10 fs due to efficient electron-electron interaction, thus increasing the overall kinetic electron energy. At 10 fs, the electron distribution has already thermalized into an M-B distribution.

The simulation thus confirms that the initial evolution of the Cu bulk is drastically out of equilibrium. Consequently, our time-integrated XAS measurements contain significant contributions from the non-equilibrium evolution stages.

Extracting the populations of the most abundant electron configurations of our model (see Fig. 4) directly connects to the spectral observations of Figs. 1 and 2. For $I = 5 \times 10^{12}$ W cm $^{-2}$, the calculated neutral species [Ar]4s 1 3d 10 abundance is $> 99\%$ and the ionization degree at the end of the pulse is $\langle Z \rangle = 0.02$. This is consistent with the low-intensity limit of the measured reference XAS spectrum (black reference in Fig. 1). For $I = 5 \times 10^{14}$ W cm $^{-2}$, we observe an abundant population of [Ar]4s 1 3d 9 of 29%, which opens up the $2p_{3/2} \rightarrow 3d$ transition and the appearance of a distinct pre-edge absorption feature. As the X-ray intensity is further increased, configurations with larger number of holes in the 3d shell are being populated, giving rise to the $2p_{3/2} \rightarrow 3d$ absorption channels of the corresponding ionic species, with blue-shifted transition energies. Consequently, the spectrum broadens and absorption increases at higher photon energies, as seen in Fig. 1 for $I = 9 \times 10^{15}$ W cm $^{-2}$. Eventually, at $I = 1 \times 10^{17}$ W cm $^{-2}$, the ground state is completely depleted, and the number of significantly populated configurations and the average ionic charge state are further increased (see lower panels of Fig. 4). The $2p_{3/2}$ ionization energy and the $2p_{3/2} \rightarrow 3d$ transition energies of these excited configurations fall out of the probed spectral range. In turn, the absorption level flattens out and the sample becomes to a large extent transparent in this spectral range.

The L_2 edge spectral region (which we describe here only qualitatively for brevity) is even more complex. Not only does it contain the $2p_{1/2} \rightarrow 3d$ absorption channels of the lowly charged ionic species, but also the $2p_{3/2} \rightarrow 3d$ channels of higher ionic species, as shown

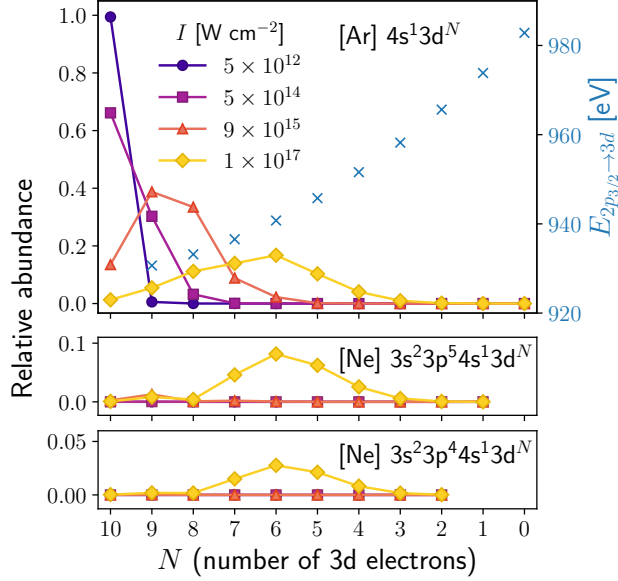


FIG. 4. Relative abundance of the most populated Cu configurations for different pulse intensities calculated with the Boltzmann kinetic model. The base configuration is shown on each panel and the number of $3d$ electrons N is varied. The blue crosses and right axis in the upper panel show the calculated energy of the $2p_{3/2} \rightarrow 3d$ transition as a function of N .

in Fig. 2 (e). Therefore, as the pulse intensity and the ionization degree are increased, $2p_{3/2} \rightarrow 3d$ absorption channels start appearing in the L_2 region, thus compensating the decrease of $2p_{1/2} \rightarrow 3d$ absorption by Cu^+ . This effect is observed in Fig. 2 by comparing the evolution of the spectral regions 1 and 4. Below the pre-edge absorption feature of L_3 (region 1), the transmission as a function of pulse intensity remains constant, within the measurement error. In contrast, the transmission in region 4 sharply decreases between $I = 5 \times 10^{15}$ and $1 \times 10^{16} \text{ W cm}^{-2}$. This sudden change is attributed to the opening of Cu^{4+} and Cu^{5+} $2p_{3/2} \rightarrow 3d$ absorption channels. These additional channels contribute to the overall absorption in the L_2 spectral region. They are the reason why the transition from RSA to SA at the L_2 edge is shifted to higher intensity compared to that at the L_3 edge.

Discussion on the pre-edge feature energy shift

Fig. 1 indicates a distinct redshift of the peak energy of the L_3 pre-edge absorption feature with increasing intensity. Its evolution is presented in Fig. 5 and shows a maximum

shift amplitude of 0.7 eV at $I = 5 \times 10^{14} \text{ W cm}^{-2}$. To interpret this shift, we first consider the simple picture of a static density of states (DOS). Upon XFEL irradiation, the 3d band is partially depopulated by the first part of the pulse via direct photoionization and electron impact ionization, starting from the most energetic electrons close to the Fermi level E_F and continuing with less energetic electrons. Consequently, as the XFEL pulse intensity is increased, the number of unoccupied 3d states probed by the remainder of the pulse increases and their average energy is reduced, thus giving rise to a pre-edge feature that increases and shifts towards lower energy, as observed.

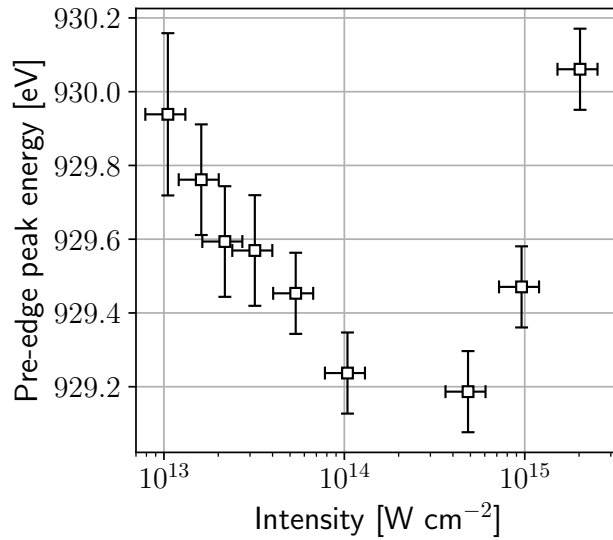


FIG. 5. Peak energy of the L_3 pre-edge absorption feature as a function of pulse intensity.

However, it has long been predicted that the transient excitation of localized 3d electrons can reduce the screening of the nucleus potential, thus shifting the Cu 3d band itself towards lower energy [22, 27, 28, 31, 38, 39]. Such a shift could, in turn, transiently increase the lattice stability by hardening the phonon modes, an effect referred to as electronic bond hardening [31, 40]. This effect is expected to be stronger when the lattice and the electrons are strongly out of equilibrium, i.e. during the early stages of WDM formation. The relation between the 3d band shift and the L_3 edge XAS spectrum is, yet, not trivial. In Ref. [22] (see Figs. 14 and 15 therein), Dorchie et al. predict that with increasing electron temperature, the pre-edge absorption feature should increase and its spectral content should shift towards lower energy, revealing the 3d band shift. In another work, the pre-edge feature energy shift is not predicted, because both the 3d and the 2p bands shift by the same amount due

to the reduction of the nucleus screening [33]. These simulations are valid for thermalized electrons with moderate temperatures: such conditions poorly compare with the highly non-equilibrium states reached in our experiment. More recently, Lee et al. [28] introduced a non-thermal electronic contribution to their density function theory (DFT) calculations and showed that the redshift of the $3d$ band grows quasi-linearly with the number of $3d$ holes per atom due to the reduction of potential screening. The considered regime is closer to what we present here and the predicted amplitude of the $3d$ band shift is in agreement with that of the presently observed pre-edge feature shift, but the time scales investigated are much longer and the resolution is limited to 200 fs. In our case, the X-ray-induced heating of materials is efficient (our Boltzmann model predicts a final temperature of ~ 7 eV at $I = 5 \times 10^{14}$ W cm^{-2}) and the achieved strongly ionizing regime was shown to lower the ionization potential [21]. Despite differences with the optically-heated WDM regime, transient band structure movements [41] and electronic bond hardening [42] are also expected and could explain the observed energy shift. This is corroborated by the observation of a similar shift at the L_2 pre-edge feature (see Fig. S5 in the Supplementary Information). Since the two edges have a similar structure, they should both be affected by the reduction of the nucleus potential screening and should manifest similar trends. Dedicated theoretical efforts are necessary to disentangle the effect of ionization potential depression from the simple depletion of the $3d$ band electrons.

Finally, with further increase of pulse intensity, and the concomitant creation of higher-charge state configurations (see Fig. 4), the central energy of the pre-edge feature shifts back to higher energies (Fig. 5).

Conclusion

We have shown that strongly focused SASE pulses from XFELs enable both the creation and the characterization of WDM via transient XAS. The method reveals in an unprecedented way the richness of the non-equilibrium electron dynamics within the material on the timescale of the X-ray pulse duration (15 fs FWHM). At moderate intensities, the localized character of the excited Cu $3d$ band and its negative energy shift is observed. At higher intensities, the transition from RSA to SA is observed and supported by our theoretical model. The latter shows the existence of non-equilibrium conditions in the electronic system and re-

lates the observations to the transient electronic state and atomic configuration occupancies of the X-ray-heated copper. While the agreement between the model and the experiment is reasonable, we note that other approaches, such as DFT, routinely used to investigate optically-heated WDM, typically assume a frozen core, a fixed density of states over time, and instantaneous electron thermalization. They are therefore inappropriate for the high pulse intensities considered here. Recent DFT calculations involving non-equilibrium two electronic temperatures [28], nonthermal lattice [43] or going beyond the frozen core approximation [42] might be future alternative approaches. Our present experimental results can be used to benchmark such theoretical developments.

The intense, nonlinear interaction induces drastic alterations of the transmitted XFEL pulse that can lead to an effective shortening of the pulse duration. The demonstration of the transition from RSA to SA further widens the applicability of X-ray pulse shaping [2, 11, 30] (see Supplementary Information for details).

The presented method uses averaged signal and reference spectra, but a self-referencing scheme could significantly increase the signal-to-noise ratio [29]. Besides, the scheme can be extended to X-ray pump – X-ray probe XAS using the two-colour mode available at current XFEL facilities [44], to follow the evolution of the WDM state in a time-resolved manner. We recall that the time resolution of our method is only limited by the pulse duration. The prospect of attosecond XFEL pulses and attosecond transient XAS capabilities will further widen the applicability of the presented approach in the study of matter under extreme conditions.

METHODS

Experimental setup. The experiment was performed at the Spectroscopy and Coherent Scattering (SCS) instrument of EuXFEL. The XFEL pulse energy was measured with two X-ray gas monitors (XGM), one located before beam transport and the other one in the SCS instrument hutch, just upstream of the focusing optics. A gas attenuator filled with adjustable N_2 pressure allowed the control of pulse energy. The beam was focused by Kirkpatrick-Báez (KB) mirrors and the beam size of $4 \mu m$ full width at half maximum was characterized by knife-edge scan. With a pulse energy of up to 2 mJ measured at the SCS XGM, an intensity of $\sim 7 \times 10^{17} \text{ W cm}^{-2}$ was achieved on sample. The accuracy of the intensity

274 reached is estimated to be $\sim 25\%$, based on the uncertainty of the XGM measurement,
 275 the transmission of the KB mirrors and the knife edge beam size characterization. A pulse
 276 duration of 15 fs FWHM was derived from spectral correlation analysis (see Supplementary
 277 Information for details). The irradiated sample was a 100 nm or 500 nm thick copper foil
 278 supported by a nickel mesh. The sample was rastered to a fresh region for every shot at the
 279 10 Hz train repetition rate of EuXFEL, and the data points where the beam hit the mesh
 280 were discarded in the analysis. The spectrometer [45] was placed 2.3 m downstream of the
 281 interaction point and consisted of an entrance slit of 40 μm and a grating with 1200 lines/mm
 282 and 5 m radius of curvature used in Rowland geometry, coupled to a CCD camera (Andor,
 283 model Newton). Energy calibration was performed using the SASE 3 monochromator [46].
 284 The low fluence limit spectra were found in good agreement with those in Refs. [25, 27]. The
 285 resolution power was $E/\Delta E \sim 2400$. To avoid saturation of the detector, attenuation of the
 286 transmitted beam was achieved with combination of Al filters of 3.5, 5 or 10 μm thickness
 287 upstream of the entrance slit of the spectrometer.

288 **Absorption spectra.** Ultrashort pulses from the European XFEL were tightly focused
 289 on a thin Cu foil and their energy tuned at the L_2 (952 eV) or L_3 (932 eV) edge, with $\sim 40\%$
 290 of their spectral content above the edge and a total bandwidth of $\sim 0.7\%$ FWHM. The
 291 spectrum of a SASE pulse contains randomly distributed spikes, such that averaging over
 292 many shots is necessary for a meaningful comparison of spectra with and without sample.
 293 Example of single shot and average spectra are shown in Fig. S1 of the Supplementary
 294 Information. For each experimental condition, a total of ~ 2000 single shot spectra without
 295 sample were recorded as well as 200 to 1000 single shot spectra with sample. The drifts
 296 of photon energy or pulse energy between two data acquisitions were small enough to be
 297 neglected. The absorption coefficient was then calculated for each photon energy as $\mu_A =$
 298 $\ln(I_{ref}/I_{Cu})/d$ where I_{ref} is the averaged reference spectrum intensity, I_{Cu} is the averaged
 299 spectrum intensity with sample and d is the sample thickness.

300 **Transmission of the XFEL pulse.** The integral over the entire SASE bandwidth of
 301 the spectra without sample, S_{ref} , or with sample, S_{Cu} , is proportional to the total number
 302 of photons of the incoming or transmitted pulse, respectively. The total transmission is thus
 303 $T = \langle S_{Cu} \rangle / \langle S_{ref} \rangle$ where $\langle \rangle$ is the average over the number of collected spectra of a given
 304 pulse intensity. Likewise, a spectrally resolved transmission can be defined within a specific
 305 photon-energy window of the spectra.

Pre-edge shift. The energy shift of the pre-edge feature was extracted by looking at the zero-crossing of the derivative of the smoothed (using Savitzky-Golay filter) absorption spectra. Given the spectrometer dispersion and the error bar in the absorption spectra, the position accuracy varies from ± 0.22 to ± 0.11 eV.

Boltzmann kinetic equations. The classical Boltzmann kinetic equations originate from the reduced N-particle Liouville equations, and include only single-particle phase-space densities of charge states and free electrons in the sample. The Boltzmann equation solver, originally constructed to follow non-equilibrium evolution of finite systems (e.g., atomic clusters) in [35] was adapted in [36] to study creation of plasma from bulk materials irradiated by X rays. In parallel, the extension of the code applicability to hard X-ray regime was performed. To circumvent the 'bottleneck' of a very high number of active configurations involved in the excitation and relaxation of the X-ray irradiated material, in [36] an alternative "predominant excitation and relaxation path" (PERP) approach was proposed. It still uses true atomic configurations but limits their number by restricting the sample relaxation to the predominant relaxation paths, determined by largest cross sections and transitions rates. The current scheme includes the most probable photoionization and the most probable Auger decay from each configuration within the path. Consistently with the treatment of only the predominant photoinduced processes, only the predominant collisional ionization processes (from the outermost shell of all considered atoms and ions) and the corresponding three-body recombination rates are modeled. They are all included in the Boltzmann collision terms. The collision terms are derived in the atomistic approximation including the interaction of isolated atoms with impact particles, and implemented within the two and three body Boltzmann collision integrals (for details see, e.g. [47, 48]). The respective cross sections and rates of atomic processes induced by X-ray photons are obtained with the XATOM code [49, 50] based on the Hartree-Fock-Slater scheme. The respective impact ionization cross sections (and the respective recombination rates) are calculated with Lotz formulas [51]. The short range electron-electron scattering are modeled with the Fokker-Planck collision integral [48]. The Pauli blocking is not included, as the electron system is assumed to be classical in this model. The modified Boltzmann equation code has been successfully applied to describe the evolution of X-ray irradiated bulk carbon and gold [36, 37].

ACKNOWLEDGEMENTS

We acknowledge European XFEL in Schenefeld, Germany, for provision of X-ray free-electron laser beamtime at Scientific Instrument SCS (Spectroscopy and Coherent Scattering) and would like to thank the staff for their assistance. We thank Alexander Reich, David Hickin and Gabriele Giovanetti for the integration of the spectrometer and Carsten Deiter for the support with the sample scanner. This work is partly supported by the Cluster of Excellence 'CUI: Advanced Imaging of Matter' of the Deutsche Forschungsgemeinschaft (DFG) - EXC 2056 - project ID 390715994. B.Z. and M.S. thank the European XFEL and the Institute of Nuclear Physics, Polish Academy of Sciences in Krakow for the support in the framework of a joint R&D project.

AUTHOR CONTRIBUTIONS

L.M., A.B., J.S. and N.R. conceived the experiment, L.M., A.B., S.K., J.S., M.A., R.C, G.F., N.G., Y.Y.K, L.L.G., G.M., S.P., J.-E.R., S.S., M.T., Z.Y., M.Z. and A.S. conducted the experiment at the SCS instrument of European XFEL, B.Z. and M.S. performed the theoretical calculations, L.M, S.K. and A.B. analyzed the data, L.M., A.B., B.Z and N.R. interpreted the data and wrote the manuscript with input from all authors.

DATA AVAILABILITY

The raw data and metadata from the experiment are available at:
<https://doi.org/10.22003/XFEL.EU-DATA-002593-00>

-
- [1] B. Nagler, U. Zastrau, R. R. Fäustlin, S. M. Vinko, T. Whitcher, A. J. Nelson, R. Sobierajski, J. Krzywinski, J. Chalupský, E. Abreu, S. Bajt, T. Bornath, T. Burian, H. Chapman, J. Cihelka, T. Döppner, S. Düsterer, T. Dzelzainis, M. Fajardo, E. Förster, C. Fortmann, E. Galtier, S. H. Glenzer, S. Göde, G. Gregori, V. Hajkova, P. Heimann, L. Juha, M. Jurek, F. Y. Khattak, A. R. Khorsand, D. Klinger, M. Kozlova, T. Laarmann, H. J. Lee, R. W. Lee, K.-H. Meiwes-Broer, P. Mercere, W. J. Murphy, A. Przystawik, R. Redmer, H. Reinholz,

- D. Riley, G. Röpke, F. Rosmej, K. Saksl, R. Schott, R. Thiele, J. Tiggesbäumker, S. Toleikis, T. Tschentscher, I. Uschmann, H. J. Vollmer, and J. S. Wark, Turning solid aluminium transparent by intense soft x-ray photoionization, [Nat. Phys. **5**, 693 \(2009\)](#).
- [2] H. Yoneda, Y. Inubushi, M. Yabashi, T. Katayama, T. Ishikawa, H. Ohashi, H. Yumoto, K. Yamauchi, H. Mimura, and H. Kitamura, Saturable absorption of intense hard X-rays in iron, [Nat. Commun. **5**, 5080 \(2014\)](#).
- [3] D. S. Rackstraw, O. Ciricosta, S. M. Vinko, B. Barbre, T. Burian, J. Chalupský, B. I. Cho, H.-K. Chung, G. L. Dakovski, K. Engelhorn, V. Hájková, P. Heimann, M. Holmes, L. Juha, J. Krzywinski, R. W. Lee, S. Toleikis, J. J. Turner, U. Zastrau, and J. S. Wark, Saturable absorption of an X-ray free-electron-laser heated solid-density aluminum plasma, [Phys. Rev. Lett. **114**, 015003 \(2015\)](#).
- [4] L. Hoffmann, S. Jamnuch, C. P. Schwartz, T. Helk, S. L. Raj, H. Mizuno, R. Mincigrucci, L. Foglia, E. Principi, R. J. Saykally, W. S. Drisdell, S. Fatehi, T. A. Pascal, and M. Zuerch, Saturable absorption of free-electron laser radiation by graphite near the carbon K-edge, [J. Phys. Chem. Lett. **13**, 8963 \(2022\)](#).
- [5] B. I. Cho, M. S. Cho, M. Kim, H.-K. Chung, B. Barbre, K. Engelhorn, T. Burian, J. Chalupský, O. Ciricosta, G. L. Dakovski, V. Hájková, M. Holmes, L. Juha, J. Krzywinski, R. W. Lee, C. H. Nam, D. S. Rackstraw, S. Toleikis, J. J. Turner, S. M. Vinko, J. S. Wark, U. Zastrau, and P. A. Heimann, Observation of reverse saturable absorption of an x-ray laser, [Phys. Rev. Lett. **119**, 075002 \(2017\)](#).
- [6] F. Kärtner, I. Jung, and U. Keller, Soliton mode-locking with saturable absorbers, [IEEE J. Sel. Top. Quantum. Electron. **2**, 540 \(1996\)](#).
- [7] G. Wang, A. A. Baker-Murray, and W. J. Blau, Saturable absorption in 2D nanomaterials and related photonic devices, [Laser Photonics Rev. **13**, 1800282 \(2019\)](#).
- [8] B. Kulyk, K. Waszkowska, A. Busseau, C. Villegas, P. Hudhomme, S. Dabos-Seignon, A. Zawadzka, S. Legoupy, and B. Sahraoui, Penta(zinc porphyrin)[60]fullerenes: Strong reverse saturable absorption for optical limiting applications, [Appl. Surf. Sci. **533**, 147468 \(2020\)](#).
- [9] X. Deng, X. Zhang, Y. Wang, Y. Song, S. Liu, and C. Li, Intensity threshold in the conversion from reverse saturable absorption to saturable absorption and its application in optical limiting, [Opt. Commun. **168**, 207 \(1999\)](#).

- [10] C. Quan, M. He, C. He, Y. Huang, L. Zhu, Z. Yao, X. Xu, C. Lu, and X. Xu, Transition from saturable absorption to reverse saturable absorption in MoTe₂ nano-films with thickness and pump intensity, *Appl. Surf. Sci.* **457**, 115 (2018).
- [11] I. Inoue, Y. Inubushi, T. Osaka, J. Yamada, K. Tamasaku, H. Yoneda, and M. Yabashi, Shortening X-ray pulse duration via saturable absorption, *Phys. Rev. Lett.* **127**, 163903 (2021).
- [12] K. Falk, Experimental methods for warm dense matter research, *High Power Laser Sci. Eng.* **6**, e59 (2018).
- [13] D. Riley, *Warm Dense Matter*, 2053-2563 (IOP Publishing, 2021).
- [14] S. M. Vinko, O. Ciricosta, B. I. Cho, K. Engelhorn, H.-K. Chung, C. R. D. Brown, T. Burian, J. Chalupský, R. W. Falcone, C. Graves, V. Hájková, A. Higginbotham, L. Juha, J. Krzywinski, H. J. Lee, M. Messerschmidt, C. D. Murphy, Y. Ping, A. Scherz, W. Schlotter, S. Toleikis, J. J. Turner, L. Vysin, T. Wang, B. Wu, U. Zastrau, D. Zhu, R. W. Lee, P. A. Heimann, B. Nagler, and J. S. Wark, Creation and diagnosis of a solid-density plasma with an x-ray free-electron laser, *Nature* **482**, 59 (2012).
- [15] S. M. Vinko, X-ray free-electron laser studies of dense plasmas, *J. Plasma Phys.* **81**, 365810501 (2015).
- [16] O. Renner and F. B. Rosmej, Challenges of x-ray spectroscopy in investigations of matter under extreme conditions, *Matter Radiat. Extrem.* **4**, 024201 (2019).
- [17] R. Alonso-Mori, D. Sokaras, M. Cammarata, Y. Ding, Y. Feng, D. Fritz, K. J. Gaffney, J. Hastings, C. C. Kao, H. T. Lemke, T. Maxwell, A. Robert, A. Schropp, F. Seiboth, M. Sikorski, S. Song, T. C. Weng, W. Zhang, S. Glenzer, U. Bergmann, and D. Zhu, Femtosecond electronic structure response to high intensity XFEL pulses probed by iron x-ray emission spectroscopy, *Sci. Rep.* **10**, 16837 (2020).
- [18] S. M. Vinko, O. Ciricosta, T. R. Preston, D. S. Rackstraw, C. Brown, T. Burian, J. Chalupský, B. I. Cho, H.-K. Chung, K. Engelhorn, R. W. Falcone, R. Fiokovini, V. Hájková, P. A. Heimann, L. Juha, H. J. Lee, R. W. Lee, M. Messerschmidt, B. Nagler, W. Schlotter, J. J. Turner, L. Vysin, Z. U., and J. S. Wark, Investigation of femtosecond collisional ionization rates in a solid-density aluminium plasma, *Nat. Commun.* **6**, 6397 (2015).
- [19] Q. Y. van den Berg, E. V. Fernandez-Tello, T. Burian, J. Chalupský, H.-K. Chung, O. Ciricosta, G. L. Dakovski, V. Hájková, P. Hollebon, L. Juha, J. Krzywinski, R. W. Lee, M. P. Minitti, T. R. Preston, A. G. de la Varga, V. Vozda, U. Zastrau, J. S. Wark, P. Velarde,

- and S. M. Vinko, Clocking femtosecond collisional dynamics via resonant x-ray spectroscopy, *Phys. Rev. Lett.* **120**, 055002 (2018).
- [20] O. Ciricosta, S. M. Vinko, H.-K. Chung, B.-I. Cho, C. R. D. Brown, T. Burian, J. Chalupský, K. Engelhorn, R. W. Falcone, C. Graves, V. Hájková, A. Higginbotham, L. Juha, J. Krzywinski, H. J. Lee, M. Messerschmidt, C. D. Murphy, Y. Ping, D. S. Rackstraw, A. Scherz, W. Schlotter, S. Toleikis, J. J. Turner, L. Vysin, T. Wang, B. Wu, U. Zastrau, D. Zhu, R. W. Lee, P. Heimann, B. Nagler, and J. S. Wark, Direct measurements of the ionization potential depression in a dense plasma, *Phys. Rev. Lett.* **109**, 065002 (2012).
- [21] O. Ciricosta, S. M. Vinko, B. Barbreil, D. S. Rackstraw, T. R. Preston, T. Burian, J. Chalupský, B. I. Cho, H.-K. Chung, G. L. Dakovski, K. Engelhorn, V. Hájková, P. Heimann, M. Holmes, L. Juha, J. Krzywinski, R. W. Lee, S. Toleikis, J. J. Turner, U. Zastrau, and J. S. Wark, Measurements of continuum lowering in solid-density plasmas created from elements and compounds, *Nat. Commun.* **7**, 11713 (2016).
- [22] F. Dorchies and V. Recoules, Non-equilibrium solid-to-plasma transition dynamics using XANES diagnostic, *Phys. Rep.* **657**, 1 (2016).
- [23] F. Dorchies, A. Lévy, C. Goyon, P. Combis, D. Descamps, C. Fourment, M. Harmand, S. Hulin, P. M. Leguay, S. Petit, O. Peyrusse, and J. J. Santos, Unraveling the solid-liquid-vapor phase transition dynamics at the atomic level with ultrafast x-ray absorption near-edge spectroscopy, *Phys. Rev. Lett.* **107**, 245006 (2011).
- [24] B. I. Cho, K. Engelhorn, A. A. Correa, T. Ogitsu, C. P. Weber, H. J. Lee, J. Feng, P. A. Ni, Y. Ping, A. J. Nelson, D. Prendergast, R. W. Lee, R. W. Falcone, and P. A. Heimann, Electronic structure of warm dense copper studied by ultrafast x-ray absorption spectroscopy, *Phys. Rev. Lett.* **106**, 167601 (2011).
- [25] B. I. Cho, T. Ogitsu, K. Engelhorn, A. A. Correa, Y. Ping, J. W. Lee, L. J. Bae, D. Prendergast, R. W. Falcone, and P. A. Heimann, Measurement of electron-ion relaxation in warm dense copper, *Sci. Rep.* **6**, 18843 (2016).
- [26] B. B. Mahieu, N. Jourdain, K. Ta Phuoc, F. Dorchies, J.-P. Goddet, A. Lifschitz, P. Renaudin, and L. Lecherbourg, Probing warm dense matter using femtosecond x-ray absorption spectroscopy with a laser-produced betatron source, *Nat. Commun.* **9**, 3276 (2018).
- [27] N. Jourdain, L. Lecherbourg, V. Recoules, P. Renaudin, and F. Dorchies, Ultrafast thermal melting in nonequilibrium warm dense copper, *Phys. Rev. Lett.* **126**, 065001 (2021).

- [28] J.-W. Lee, M. Kim, G. Kang, S. M. Vinko, L. Bae, M. S. Cho, H.-K. Chung, M. Kim, S. Kwon, G. Lee, C. H. Nam, S. H. Park, J. H. Sohn, S. H. Yang, U. Zastrau, and B. I. Cho, Investigation of nonequilibrium electronic dynamics of warm dense copper with femtosecond x-ray absorption spectroscopy, [Phys. Rev. Lett. **127**, 175003 \(2021\)](#).
- [29] M. Harmand, M. Cammarata, M. Chollet, A. G. Krygier, H. T. Lemke, and D. Zhu, [Single-shot x-ray absorption spectroscopy at x-ray free electron lasers](#) (2020), arXiv:2005.01572.
- [30] M. S. Cho, H.-K. Chung, and B. I. Cho, Intensity-dependent resonant transmission of x-rays in solid-density aluminum plasma, [Phys. Plasmas **25**, 053301 \(2018\)](#).
- [31] V. Recoules, J. Cl  rouin, G. Z  rah, P. M. Anglade, and S. Mazevet, Effect of intense laser irradiation on the lattice stability of semiconductors and metals, [Phys. Rev. Lett. **96**, 055503 \(2006\)](#).
- [32] L. Van Hove, The occurrence of singularities in the elastic frequency distribution of a crystal, [Phys. Rev. **89**, 1189 \(1953\)](#).
- [33] N. Jourdain, V. Recoules, L. Lecherbourg, P. Renaudin, and F. Dorchies, Understanding XANES spectra of two-temperature warm dense copper using ab initio simulations, [Phys. Rev. B **101**, 125127 \(2020\)](#).
- [34] B. Henke, E. Gullikson, , and J. Davis, X-ray interactions: photoabsorption, scattering, transmission, and reflection at E=50-30000 eV, Z=1-92, *At. Data Nucl. Data Tables* **54**, 181 (1993).
- [35] B. Ziaja, A. R. D. Castro, E. Weckert, and T. M  ller, Modelling dynamics of samples exposed to free-electron-laser radiation with Boltzmann equations, [Eur. Phys. J. D **40**, 465 \(2006\)](#).
- [36] B. Ziaja, V. Saxena, S.-K. Son, N. Medvedev, B. Barbre  l, B. Woloncewicz, and M. Stransky, Kinetic Boltzmann approach adapted for modeling highly ionized matter created by x-ray irradiation of a solid, [Phys. Rev. E **93**, 053210 \(2016\)](#).
- [37] B. Ziaja, J. J. Beks, M. Masek, N. Medvedev, P. Piekarczyk, V. Saxena, M. Stransky, and S. Toleikis, Tracing X-ray-induced formation of warm dense gold with Boltzmann kinetic equations, [Eur. Phys. J. D **75**, 224 \(2021\)](#).
- [38] E. B  villon, J. P. Colombier, V. Recoules, and R. Stoian, Free-electron properties of metals under ultrafast laser-induced electron-phonon nonequilibrium: A first-principles study, [Phys. Rev. B **89**, 115117 \(2014\)](#).
- [39] N. Jourdain, L. Lecherbourg, V. Recoules, P. Renaudin, and F. Dorchies, Electron-ion thermal equilibration dynamics in femtosecond heated warm dense copper, [Phys. Rev. B **97**, 075148](#)

(2018).

- [40] R. Ernstorfer, M. Harb, C. T. Hebeisen, G. Sciaini, T. Dartigalongue, and R. J. D. Miller, The formation of warm dense matter: Experimental evidence for electronic bond hardening in gold, *Science* **323**, 1033 (2009).
- [41] J. J. Bekx, S.-K. Son, B. Ziaja, and R. Santra, Electronic-structure calculations for nonisothermal warm dense matter, *Phys. Rev. Res.* **2**, 033061 (2020).
- [42] Q. Zhang, X. Yu, Q. Zeng, H. Zhang, S. Zhang, C. Gao, D. Kang, J. Wu, and J. Dai, Effect of nonequilibrium transient electronic structures on lattice stability in metals: Density functional theory calculations, *Front. Phys.* **10**, 838568 (2022).
- [43] L. Waldecker, R. Bertoni, R. Ernstorfer, and J. Vorberger, Electron-phonon coupling and energy flow in a simple metal beyond the two-temperature approximation, *Phys. Rev. X* **6**, 021003 (2016).
- [44] S. Serkez, W. Decking, L. Froehlich, N. Gerasimova, J. Grünert, M. Guetg, M. Huttula, S. Karabekyan, A. Koch, V. Kocharyan, Y. Kot, E. Kukk, J. Laksman, P. Lytaev, T. Maltezopoulos, T. Mazza, M. Meyer, E. Saldin, E. Schneidmiller, M. Scholz, S. Tomin, M. Vannoni, T. Wohlenberg, M. Yurkov, I. Zagorodnov, and G. Geloni, Opportunities for two-color experiments in the soft x-ray regime at the European XFEL, *Appl. Sci.* **10**, 2728 (2020).
- [45] J. Nordgren, G. Bray, S. Cramm, R. Nyholm, J.-E. Rubensson, and N. Wassdahl, Soft x-ray emission spectroscopy using monochromatized synchrotron radiation, *Rev. Sci. Instrum.* **60**, 1690 (1989).
- [46] N. Gerasimova, D. La Civita, L. Samoylova, M. Vannoni, R. Villanueva, D. Hickin, R. Carley, R. Gort, B. E. Van Kuiken, P. Miedema, L. Le Guyader, L. Mercadier, G. Mercurio, J. Schlappa, M. Teichman, A. Yaroslavtsev, H. Sinn, and A. Scherz, The soft X-ray monochromator at the SASE3 beamline of the European XFEL: from design to operation, *J. Synchrotron Radiat.* **29**, 1299 (2022).
- [47] V. V. Aristov, *Direct Methods for Solving the Boltzmann Equation and Study of Nonequilibrium Flows* (Springer Dordrecht, 2001).
- [48] I. P. Shkarofsky, T. W. Johnston, and M. P. Bachynski, The particle kinetics of plasmas, *Am. J. Phys.* **35**, 551 (1967).
- [49] S.-K. Son, L. Young, and R. Santra, Impact of hollow-atom formation on coherent x-ray scattering at high intensity, *Phys. Rev. A* **83**, 033402 (2011).

- 516 [50] Z. Jurek, S.-K. Son, B. Ziaja, and R. Santra, *XMDYN* and *XATOM*: versatile simulation tools
517 for quantitative modeling of X-ray free-electron laser induced dynamics of matter, [J. Appl.](#)
518 [Crystallogr.](#) **49**, 1048 (2016).
- 519 [51] W. Lotz, Electron-impact ionization cross-sections for atoms up to $Z=108$, [Z. Phys.](#) **232**, 101
520 [\(1970\)](#).

Supplementary Files

This is a list of supplementary files associated with this preprint. Click to download.

- [supplementaryinformation20221220.pdf](#)
- [supplementaryinformation20221220.pdf](#)